# Application of an optical hydrophone to ionoacoustic range detection in a tissue-mimicking agar phantom

**Running title:** Ionoacoustic range detection of protons

Shota Sueyasu[1], Koki Kasamatsu[2,3], Taisuke Takayanagi[4], Ye Chen[5], Yasutoshi Kuriyama[6], Yoshihiro Ishi[6], Tomonori Uesugi[6], Wolfgang Rohringer[7], Mehmet Burcin Unlu[5,8], Nobuki Kudo[9], Kohei Yokokawa[5,10], Seishin Takao[5,10], Naoki Miyamoto[5,10], Taeko Matsuura[5,10]

[1]Graduate School of Engineering, Hokkaido University, North-13 West-8, Kita-ku, Sapporo, Hokkaido, 060-8628, Japan

[2]Graduate School of Biomedical Science and Engineering, Hokkaido University, Sapporo, Hokkaido, 060-0814, Japan

[3]Institute for Quantum Medical Science, Quantum Life and Medical Science Directorate, National Institutes for Quantum Science and Technology (QST), 4-9-1 Anagawa, Inage-Ku, Chiba, 263-8555, Japan

[4]Hitachi Ltd, Research and Development Group, Center for Technology Innovation-Energy, Hitachi-shi, Ibaraki, 319-1292, Japan

[5]Faculty of Engineering, Hokkaido University, North-13 West-8, Kita-ku, Sapporo, Hokkaido, 060-8628, Japan

[6]Institute for Integrated Radiation and Nuclear Science, Kyoto University, Osaka, 590-0494, Japan

[7]XARION Laser Acoustics GmbH, Ghegastraße 3, 1030, Vienna, Austria

[8]Department of Physics, Bogazici University, Bebek, Istanbul, 34342, Turkey

[9]Faculty of Information Science and Technology, Hokkaido University, North-14, West-9, Kita-ku, Sapporo, Hokkaido, 060-0814, Japan

[10]Department of Medical Physics, Hokkaido University Hospital, North-15 West-7, Kita-ku, Sapporo, Hokkaido, 060-8638, Japan

***Corresponding author:** Dr. Taeko Matsuura, Faculty of Engineering, Hokkaido University, North-15 West-7, Kita-ku, Sapporo, Hokkaido, 060-8638, Japan. Tel: +81-11-706-5254; Email: matsuura@med.hokudai.ac.jp

*Abstract*

Background: Ionoacoustics is a promising approach to reduce the range uncertainty in proton therapy. A miniature-sized optical hydrophone (OH) was used as a measuring device to detect weak ionoacoustic signals with a high signal-to-noise ratio in water. However, further development is necessary to prevent wave distortion because of nearby acoustic impedance discontinuities while detection is conducted on the patient's skin.

Purpose: A prototype of the probe head attached to an OH was fabricated and the required dimensions were experimentally investigated using a 100-MeV proton beam from a fixed-field alternating gradient accelerator and k-Wave simulations. The beam range of the proton in a tissue-mimicking phantom was estimated by measuring γ-waves and spherical ionoacoustic waves with resonant frequency (SPIRE).

Methods: Four sizes of probe heads were fabricated from agar blocks for the OH. Using the prototype, the γ-wave was detected at distal and lateral positions to the Bragg peak on the phantom surface for proton beams delivered at seven positions. For SPIRE, independent measurements were performed at distal on- and off-axis positions. The range positions were estimated by solving the linear equation using the sensitive matrix for the γ-wave and linear fitting of the correlation curve for SPIRE; they were compared with those measured using a film.

Results: The first peak of the γ-wave was undistorted with the $3 \times 3 \times 3$-cm$^3$ probe head used at the on-axis and 3-cm off-axis positions. The range positions estimated by the γ-wave agreed with the film-based range in the depth direction (the maximum deviation was 0.7 mm), although a 0.6–2.1 mm deviation was observed in the lateral direction. For SPIRE, the deviation was <1 mm for the two measurement positions.

Conclusions: The attachment of a relatively small-sized probe head allowed the OH to measure the beam range on the phantom surface.

## 1. Introduction

Range uncertainty of proton beams when applied to patients has been a key issue in proton therapy that could offset the potential advantage of protons in delivering a conformed dose to target tumors. Ionoacoustics, or protoacoustics, is a promising approach that is used to recover dose conformity by identifying the beam range or reconstructing the dose distribution in real time via the detection of the thermoacoustic waveform emitted from the region of dose deposition.[1,2,3] In contrast to nuclear-interaction-based techniques, such as prompt gamma detection and positron emission tomography, ionoacoustics can use detectors as compact as several centimeters or millimeters.[4-18] Therefore, it is easier to use with imaging modalities such as X-ray fluoroscopy[19] and MRI scanners[20] deployed close to patients. Additionally, ionoacoustics has an advantage in conjunction with high-dose-rate irradiation, which is being investigated in the context of FLASH, as the acoustic pressure signal is increased at a high beam current.[7]

Because of the nature of the Bragg curve, two types of ionoacoustic waves are emitted from the proton beam: a cylindrical wave from the plateau region ($\alpha$-wave) and a quasi-spherical wave from the Bragg peak ($\gamma$-wave). Generally, the observed wave is the superposition of these two waves and both have a frequency range of around 100 kHz. Additionally, for several treatment sites, fiducial markers made of metals are inserted into tissues for patient positioning. When the proton beams pass through the spherical-shaped markers, an omnidirectional ionoacoustic wave referred to as spherical ionoacoustic waves with resonant frequency (SPIRE) is emitted from the marker.[8] For instance, with a marker made of gold and a 2-mm diameter, the resonance was observed at 1.53 MHz. Both $\gamma$-waves and SPIRE can be used for range detection in unique ways.[8,9]

Currently, most research conducted with preclinical[4-7,17,18] and clinical systems[7,10-14] has employed piezoelectric hydrophones (PH) with a few exceptions.[9] For these devices, the detector thickness optimum for ionoacoustic range detection would be several centimeters because the piezo material thickness is inversely correlated to the center frequency, and several centimeters of the sensitive area is required to detect the weak ionoacoustic waves with a high signal-to-noise ratio (SNR).[16] Although the size is still small, it can distort ionoacoustic waves by averaging over the sensitive area.[6] Additionally, PH can make shadows in the fluoroscopy images which can be an obstacle in tracking tumors or fiducial markers when the projected images of hydrophones overlap with the images of tumors or markers. The optical hydrophone (OH) is advantageous in this regard because its sensitivity depends on the efficiency with which acoustic perturbations are converted into changes in light characteristics in the sensing system and is independent of the detector size.[21] Moreover, its projected image in fluoroscopy images was shown to be almost negligible.[9] Previously, we used a millimeter-sized OH to demonstrate γ-wave detection in a water phantom with clinical dosage.[9] For the SPIRE measurement, although the sensitivity was low, it was observed that the robustness to detector setup errors was greater than that found with a PH because of the small size of the sensitive volume of the OH.

Meanwhile, further development is required for OH measurement of ionoacoustic signals with a patient. Measurement performed in a water phantom does not distort the initial segment of the ionoacoustic wave, although echoes from the sensor element and frame will subsequently distort the waveform. However, if the sensor is placed with an acoustic gel directly onto the skin of the patient, the initial segment is distorted by the waves reflected by the sensor-air boundary, which prohibits the extraction of the necessary information from waveforms (See the Supplementary Material for the typical wave distortion with the direct coupling). Therefore, this study aims to construct a method to measure the beam range in a tissue-mimicking phantom using OH. We propose a prototype design of the probe head for OH that prevents wave distortion for γ-wave and SPIRE. Using the prototype, we detected the γ-wave and SPIRE on the surface of the tissue-mimicking agar phantom and investigated the range accuracy using the sensitive matrix method for the γ-wave and linear interpolation of the resonance intensities for SPIRE.

## 2. Material and Methods

### 2.1 Experiment

The experiments were performed using a 100-MeV pulsed proton beam from a fixed-field alternating gradient accelerator (Kyoto University).[22,23] The setup of the tissue-mimicking phantom, probe heads, proton beam, and a gold marker (GM) for the SPIRE measurement are demonstrated in Figure 1. Three holes were made in the acrylic container containing the phantom for the passage of the proton beam and probe head installation. The probe head was coupled to the phantom with an acoustic gel and set at distal and lateral positions, downstream of the Bragg peak. Instead of scanning the beam, the phantom and probe heads were moved from $X = -30$ to $+30$ mm using the $XY$-translation stage. A plastic scintillator coupled to a photomultiplier tube was set at the exit of the beam duct to measure the temporal pulse width and beam-on timing.

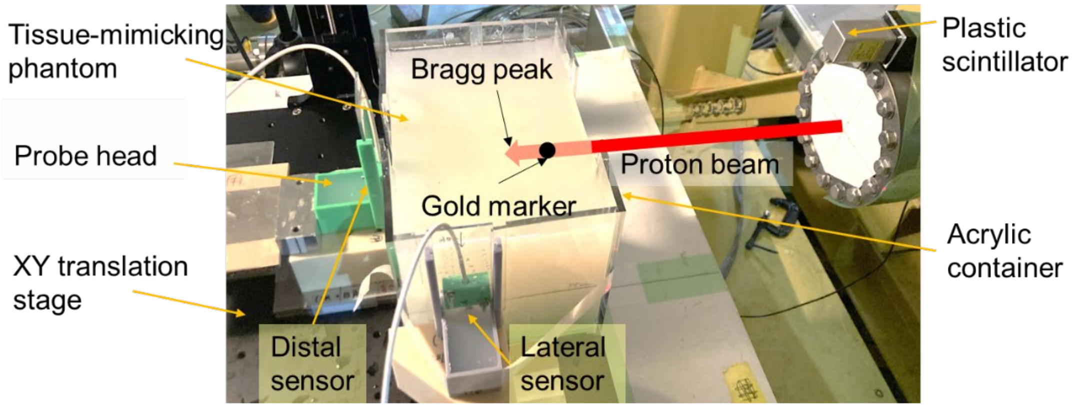


Figure 1. Photograph of the experimental setup. A 100-MeV proton beam bombarded the tissue-mimicking phantom through a hole in the acrylic container. The phantom and probe head were set on the $XY$-translation stage while GM was set on the beam axis. A plastic scintillator was placed at the exit of the beam duct.

The dimensions of the phantom and coordinates of probe heads and GM are demonstrated in Figure 2; (*X, Y, Z*) refers to a coordinate system fixed to the phantom. Measurements were performed in the same plane as the proton beam (*XZ* plane). First, the γ-wave and SPIRE were measured by the distal sensor with four sizes of probe heads (2 × 2 × 2, 3 × 3 × 3, 3 × 3 × 6, and 5 × 5 × 8 $cm^3$). Then, by using the 3 × 3× 6-$cm^3$ prototype, the range position was identified with multiple beams. For the range detection using γ-waves, a total of seven proton beams incident at $X = -30, -20, -10, 0, +10, +20$, and $+30$ mm were tested (Figure 2 (a)). The phantom and the probe head, placed at distal and lateral positions were set on the *XY*-translation stage and aligned to the beam incident at $X = 0$ using a laser marker. The stage potentiometer was set to zero at $X = 0$ and moved at a 10-mm pitch from $X = -30$ to $+30$ mm. By contrast, for the range detection using SPIRE, a proton beam incident at $X = 0$ was tested at two respective sensor positions, $(X, Z) = (0, 134)$ and $(29, 134)$ (mm) (Figure 2 (b)). As the range detection via SPIRE requires at least two measurements using range shifters,[8,9] we placed acrylic plates (relative stopping power of 1.16) of several thicknesses (<14 mm) in front of the phantom (Figure 2 (b)).

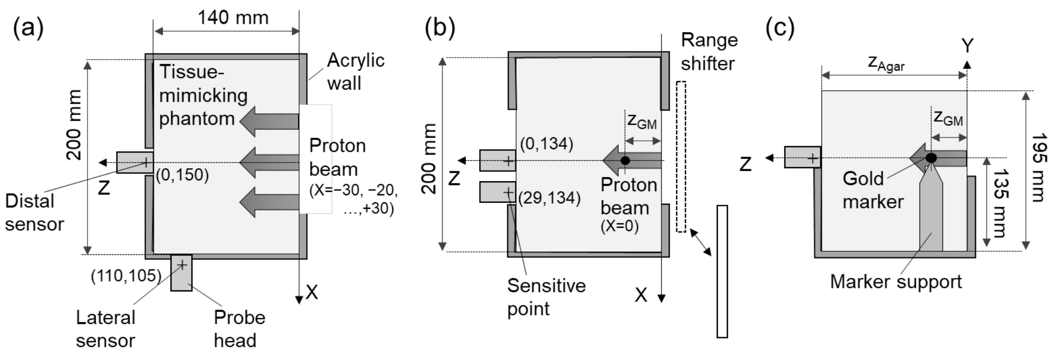


Figure 2. (a) Top view of the tissue-mimicking phantom and probe head setup for the γ-wave measurement, and (b) top view and (c) side view of the SPIRE measurement. (*X, Y, Z*) is a coordinate system fixed to the phantom. Crosses indicating the sensitive point (center of the sensitive volumes) and the coordinates (*X, Z*) are shown together (unit: mm). Tested proton beams are illustrated by the arrows. For the γ-wave measurement, the phantom was shifted by the translation stage in the *X*-direction, whereas for SPIRE measurement, the phantom was fixed, and the probe head was shifted by hand. $z_{Agar}$ and $z_{GM}$ depend on the Run and are shown in Table 1.

As in our previous study,[9] the lateral beam size and range were measured by using a radiochromic film EBT3 (Ashland Inc., Wayne, New Jersey, USA). The correlation between the proton number per pulse and the scintillator signal height was measured with a Faraday cup before the experiment, and during the ionoacoustic measurement, the scintillator signal was used to estimate the proton number per pulse. The beam range, temporal pulse width, lateral beam size, and protons/pulse are summarized in Table 1. Three separate experiments (Run 1, 2, and 3) were performed at an interval of about half a year. FFA parameters were adjusted to achieve similar beam conditions for all experiments.

A total of 1,000 signals were individually recorded per measurement condition. We observed the electromagnetic noise emitted from the beam extraction kicker of the FFA accelerator; however, as it always had the same shape, it could be completely subtracted from the signal. The measured signal was processed by low (<150 kHz) and bandpass (1.53 MHz) filters for γ-wave and SPIRE, respectively, and amplified by 40 dB.

Table 1. Summary of phantom size and beam characteristics.

| Run | Measured wave | Experiment description | Phantom depth size (mm) [b] | GM position (mm) [c] | Beam range (mm) [d] | Pulse width (ns) | Beam size (mm) [d],[e] | Bragg peak dose /pulse (Gy) [f] | Protons/ pulse |
|---|---|---|---|---|---|---|---|---|---|
| 1 | γ-wave | PHC,<br>RD [a] | 140 | - | 73.8 | 30 | 5.1(*X*)<br>4.5(*Y*) | 0.3 | 1.1–1.3 $\times 10^8$ |
| 2 | SPIRE | PHC | 123 | 63 | 73.8 | 30 | 5.1(*X*)<br>4.5(*Y*) | 0.3 | 1.1–1.3 $\times 10^8$ |
| 3 | | RD | 124 | 60 | 73.9 | 22 | 3.1(*X*)<br>2.8(*Y*) | 0.7 | $7.2 \times 10^7$ |

[a]PHC: probe head size comparison, RD: range detection. [b]$z_{Agar}$ in Figure 2. [c]$z_{GM}$ in Figure 2. [d]Range and beam size measured by the film. [e]Beam sizes in the table are the values at the entrance of the phantom. [f]The Bragg peak dose was calculated via the Monte Carlo simulation Geant4 (Sec. 2.4).

*2.2 Phantom*

An agar-based soft tissue-mimicking phantom was prepared in the acrylic container. Agarose powder (Fujifilm Wako Pure Chemical Industries, Ltd, Japan) was used at 1% weight per volume. After the agarose had solidified overnight, holes were made in the acrylic wall to produce spare space for the beam transmission and probe head. Table 1 summarizes the phantom size. The phantom was prepared for each experiment to prevent corrosion. GM with a 2-mm diameter was embedded in the agar phantom at a distance of 63 and 60 mm (Run 2 and 3, respectively) from the beam incident surface. The marker was set on the tip of a pencil-shaped support made of ABS.[8] The speed of sound in the agar phantom was measured using the pulser/receivers (Model 5072 PR, Olympus NDT Inc., USA) on the day of each experiment by the pulsed echo method and was found to be 1,476 m/s for Run 1 and 2 and 1,492 m/s for Run 3. The variation in the sound speed may be attributed to the different amounts of water vaporized during the preparation process.

*2.3 OH and probe head design*

An Eta250 L Ultra (XARION Laser Acoustics GmbH, Vienna, Austria) was used for the OH.[24] This was a Fabry-Perot resonator, and the sensitive volume size was defined by the laser beam diameter (0.35 mm) and mirror distance (2 mm). The sensor head was embedded in agar blocks of various sizes ($x_{PH}, y_{PH}, z_{PH}$) = (2, 2, 2), (3, 3, 3), (3, 3, 6), and (5, 5, 8) cm$^3$ to produce a water-like environment around the sensor head (Figure 3 (a)). The first positive peak of the γ-wave arrives within 10 μs (wave traveling distance of 1.5 cm) after the initial rise in all experiments; therefore, the minimum distance between the sensor head and back wall of the probe head was set to 1 cm to prevent the wave from being affected by acoustic echoes. In the γ-wave measurement, the positioning accuracy of the sensor head directly affects the range accuracy. To install the sensor head accurately at the designed position, we fabricated a 3D-printed probe head frame. The sensor head was set at 1 cm from the front of the probe head surface using a guide and the probe head surface was aligned with the inner surface of the acrylic encasing of the agar phantom using a stopper (Figure 3 (b)).

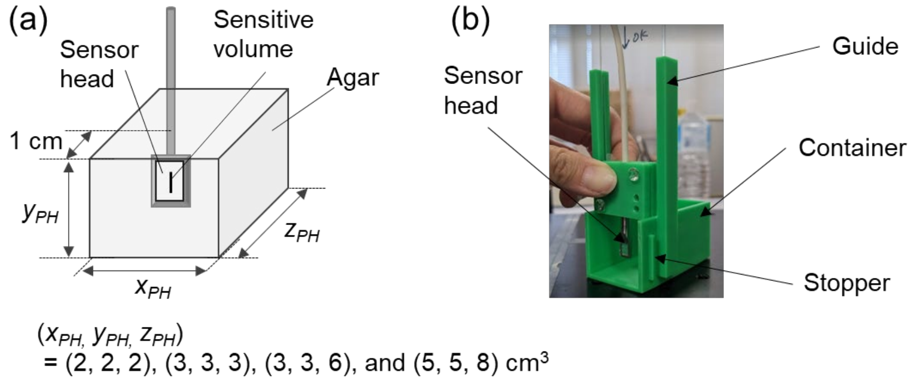


Figure 3. (a) Dimensions of the agar block of the probe head. The sensor head of the OH is embedded in the agar block at a 1-cm depth from the front surface. (b) The 3D-printed probe head frame, made of ABS, and the sensor head. A guide is used to fix the sensor head at 1 cm from the front surface of the probe head. A stopper is used to align the probe head surface with the inner wall of the acrylic encasing of the agar phantom.

*2.4 Acoustic wave transport simulation*

The simulation was performed for two reasons. First, our range detection method requires the simulated waveform. Second, as denoted in Sec. 2.1 the probe head size comparison measurement was performed only at the distal position. Since the probe head size dependence can vary at different positions as the waveform changes, the investigation was expanded to a wider range of positions (Figure 4) using simulations.

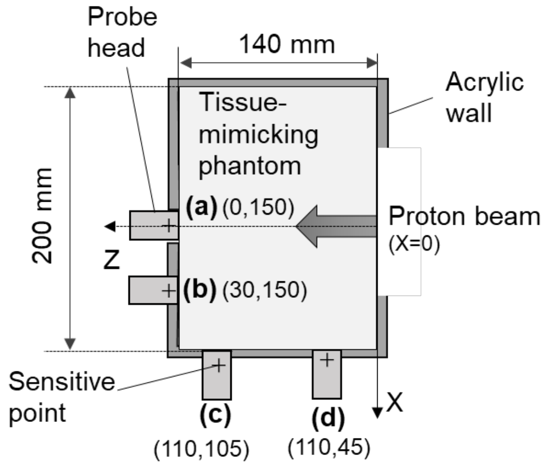


Figure 4. Simulation geometry of the probe head size dependence with dimension in millimeters. (a)–(d) are the simulated sensor positions. In addition to (a), which was experimentally investigated, three positions were investigated using simulation.

The simulation used Geant4 (ver. 10.6.2)[25] and MATLAB toolbox k-Wave.[26] The initial beam parameters of the Geant4 Monte Carlo simulation were adjusted to reproduce the beam properties measured by the film (beam range and in-air beam profiles at three depths). The 3D distributions of transferred energy in agar phantom, $E(\vec{r})$, were calculated and used as the source pressure in the acoustic wave transport simulation k-Wave. The following wave equation was solved:

$$\frac{1}{v^2}\frac{\partial^2 p}{\partial t^2} - \nabla^2 p = (\Gamma/v^2)E(\vec{r})I'(t)$$

where $I'(t)$ denotes the time derivative of the normalized beam current. The Grüneisen coefficient of the agar, $\Gamma$, was set to 0.11, and the sound velocity of the agar and air, $v$, was set to 1,476 and 340 m/s, respectively. As the pulse temporal width of the fixed-field alternating gradient accelerator (≤30 ns) was sufficiently shorter than the characteristic time scale of γ-wave (~ μs), the simulation was performed with the impulse source in time, i.e., $I(t) = \delta(t)$. The voxel size was 0.33 mm in all dimensions, and the time step was 10 ns. The probe head was modeled as rectangular boxes. During the simulation, we replaced the 2-mm thick ABS container of the probe head with air. As shown in the Supplementary Material, although the inclusion of the ABS container can slightly affect the waveform, it does not change the first peak arrival time at any measurement position. For simplicity, the internal structure of the sensor head was not modeled and the sensor was assumed to be a point with a flat frequency response.

*2.5 Range detection methods*

The following range detection methods were adopted for γ-waves and SPIRE. The range positions measured by the ionoacoustics may differ from those measured by the film and potentiometer of the stage because of the residual positioning error of the phantom and probe head (and GM positioning error in the case of SPIRE), as well as limited accuracy of the simulations. We defined this deviation as $(\Delta X, \Delta Z)$, and determined its value for each tested beam. For simplicity, $\Delta Y$ was assumed to be zero throughout the measurement.

*2.5.1 γ-wave*

The range position in the *XZ* plane was estimated from the first peak arrival times of γ-waves (referred to as $t_{\gamma}^{peak}$) measured at distal and lateral positions in the *XZ* plane (Figure 2 (a)), defined as $\boldsymbol{t^{exp}} = \left(t_{dist}^{exp}, t_{lat}^{exp}\right)^{T}$, where *T* indicates the "transposed." Using Geant4, the dose distributions in the phantom were calculated where the range positions were adjusted to $\boldsymbol{X^{sim}} = \left(X^{sim}, Z^{sim}\right)^{T}$ ($X^{sim} = -30, -20, -10, 0, +10, +20, +30$ mm, $Z^{sim} = 73.9$ mm). Here, the values of $X^{sim}$ were those indicated by the potentiometer and the $Z^{sim}$ was the beam range measured by the film. Then, by using the acoustic wave transport simulation, $t_{\gamma}^{peak}$ at distal and lateral positions, $\boldsymbol{t^{sim}} = \left(t_{dist}^{sim}, t_{lat}^{sim}\right)^{T}$, and the sensitive matrix defined by

$$S = \begin{pmatrix} \dfrac{\partial t_{dist}^{sim}}{\partial X} & \dfrac{\partial t_{dist}^{sim}}{\partial Z} \\ \dfrac{\partial t_{lat}^{sim}}{\partial X} & \dfrac{\partial t_{lat}^{sim}}{\partial Z} \end{pmatrix}$$

were calculated. For instance, the (1, 1) component of the matrix element indicates the increased rate of the $t_{\gamma}^{peak}$ observed at distal sensor with the positive beam shift in *X*-direction. Then the range position detected using γ–wave was derived by $\boldsymbol{X}^{\boldsymbol{exp}} = \boldsymbol{X}^{\boldsymbol{sim}} + \Delta\boldsymbol{X}$, where $\Delta\boldsymbol{X} = (\Delta X, \Delta Z)^T = \boldsymbol{S}^{-\boldsymbol{1}}\Delta\boldsymbol{t}, \Delta\boldsymbol{t} = \boldsymbol{t}^{\boldsymbol{exp}} - \boldsymbol{t}^{\boldsymbol{sim}}$. In addition to this, $\Delta Z$ was derived using a single distal sensor from $\Delta Z = \left(\frac{\partial t_{dist}^{sim}}{\partial Z}\right)^{-1} \Delta t_{dist}$.

### 2.5.2 SPIRE

For SPIRE, the range detection method proposed in a previous study was used.[9] This method can only detect the range error in the *Z* direction. In brief, the waveform in the time domain was first converted to the frequency domain by a fast Fourier transform, and the signal intensities at the resonance frequency measured with different thicknesses of acrylic plates were plotted in terms of the distance between the GM and the beam range measured by the film. The data points were fitted by using a linear function, and the intersection point with the horizontal axis was compared with that obtained from the wave transport simulation. The difference was identified as $\Delta Z$. In this study, the intersection point of the simulation was assumed to be the same as in the previous study (-1.1 mm).

## 2.6 Evaluation

We first compared $t_{\gamma}^{peak}$ and peak pressures of the γ–waves among four probe head sizes. A comparison was made with an experiment at the distal position and simulations at all sensor positions in Figure 4. The experiment was also conducted for the SPIRE at the distal position, and the variation in $\Delta Z$ among four probe head sizes was evaluated. Then, using 3 × 3 × 6- $cm^3$ probe head, the range position was identified for proton beams delivered at seven positions using γ-waves and for a beam using SPIRE.

## 3. Results

### 3.1 Probe head size

#### 3.1.1 γ-wave

Figure 4 shows the γ-waves detected by four sizes of probe heads placed at distal position. The signal amplitude was normalized by the number of particles per pulse. The first positive peak shape and $t_{\gamma}^{peak}$ were in good agreement among different probe head sizes, and the maximum variation of the arrival times was 0.3 μs (0.45 mm in wave propagation distance). The waveforms started to deviate from each other after the intersection point with the time-axis (arrow in Figure 5).

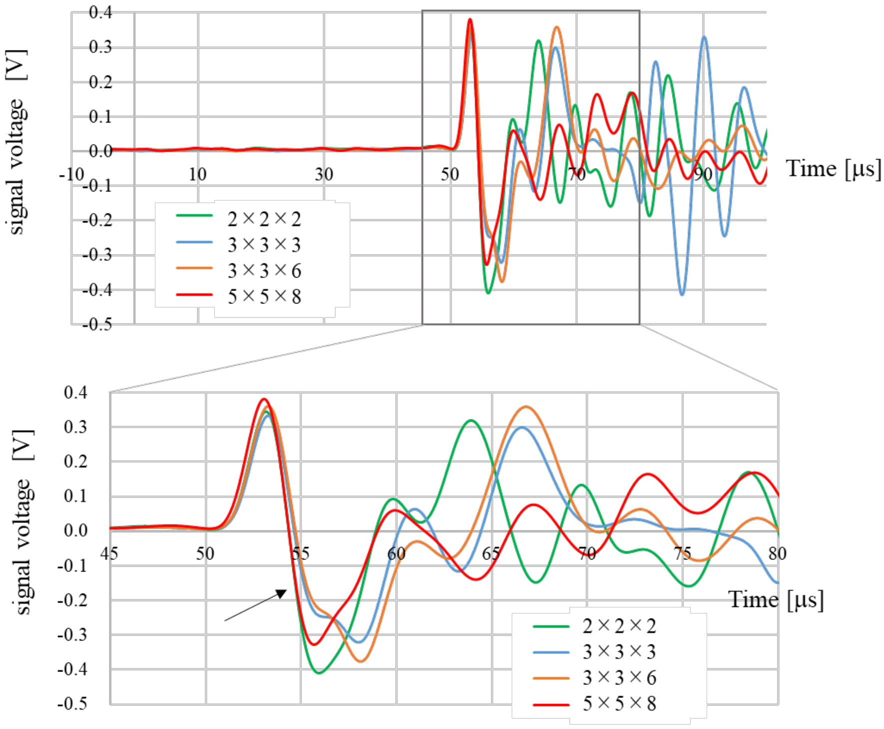


Figure 5. Measured waveforms of the γ-waves incident from X = 0 among different sizes of probe heads placed at the distal position with an experimental setup of Figure 2 (a) (1000-fold averaging). The figure below shows an enlarged view of the time range from 45 to 80 μs.

Figure 6 shows a comparison of simulated waveforms at the various sensor positions described in Figure 4. As a reference, the waveforms resulting from a water phantom environment model are shown together. The simulation result of position (a) agreed with the experimental result (Figure 5) in that the first peak shapes of all probe heads were similar. In all tested positions, $t_{\gamma}^{peak}$ and the peak pressure of the 5 × 5 × 8-cm$^3$ probe head agreed with that obtained in the water phantom environment, whereas deviation was observed for other probe heads. For example, with the smallest probe head of 2 × 2 × 2 cm$^3$, a deviation of $t_{\gamma}^{peak}$ was observed at both the distal and lateral positions; moreover, the peak pressure decreased by approximately 10% and 70% at (b) and (c), respectively. With both the 3 × 3 × 3- and 3 × 3 × 6-cm$^3$ probe heads, the peak arrives 1 μs ahead of the water-like environment and a mild decrease of the peak pressure (30%) was observed at position (c). At all tested positions, the initial segment of the waveforms of the 3 × 3 × 3- and 3 × 3 × 6-cm$^3$ probe heads agreed with each other.

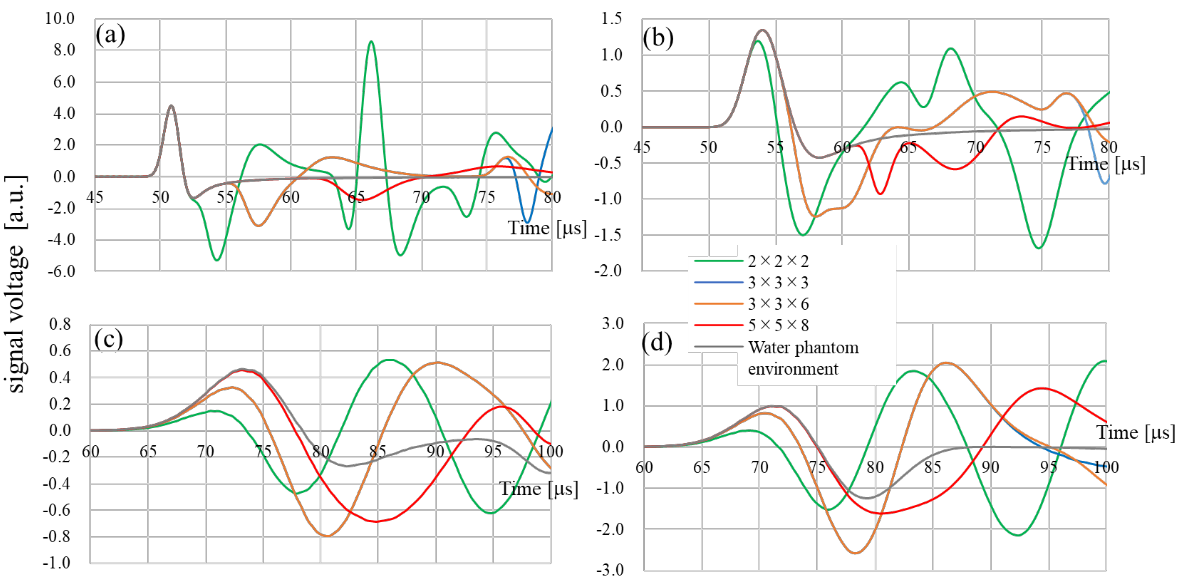


Figure 6. Simulated waveforms obtained with different sizes of probe heads at various positions relative to the proton beam. (a)−(d) indicate the waveforms obtained by the (a)–(d) positions in Figure 4. Green, blue, orange, and red curves show the simulations with 2 × 2 × 2, 3 × 3 × 3, 3 × 3 × 6, and 5 × 5 × 8-cm$^3$ probe head, respectively. Gray curves show the waveforms resulting from a water phantom environment model.

*3.1.2 SPIRE*

Figure 7 shows the SPIRE waveforms measured by the different sizes of probe heads. The resonance wave was observed even with the smallest 2 × 2 × 2-cm$^3$ probe head. By converting these waveforms in the time interval of 40–90 µs to the frequency domain by fast Fourier transform, the resonance was observed at 1.58–1.60 MHz. Figure 8 shows the signal intensities at the resonance frequency, plotted in terms of the distance between the GM and the beam range predicted by the film. The maximum variation of $\Delta Z$ among different probe head sizes, estimated from the intersection points of the fitted linear lines and the *x*-axis (indicated by an arrow in the figure), was only 0.2 mm. The resonance intensity did not vary considerably among different probe heads, probably because the echoes in the detector's internal structure are dominant over the reflected waves from nearby impedance discontinuities.

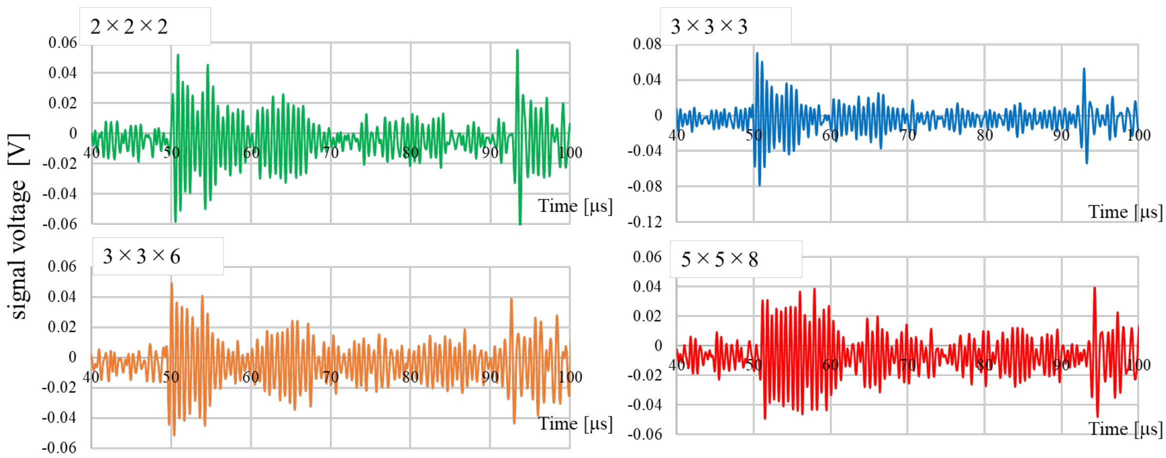


Figure 7. SPIRE waveforms observed with four sizes of probe head (1,000-fold averaging). The SPIRE starts from approximately 50 µs. The large amplitude commonly observed at approximately 95 µs is the reflected wave of SPIRE at the upper surface of the agar phantom.

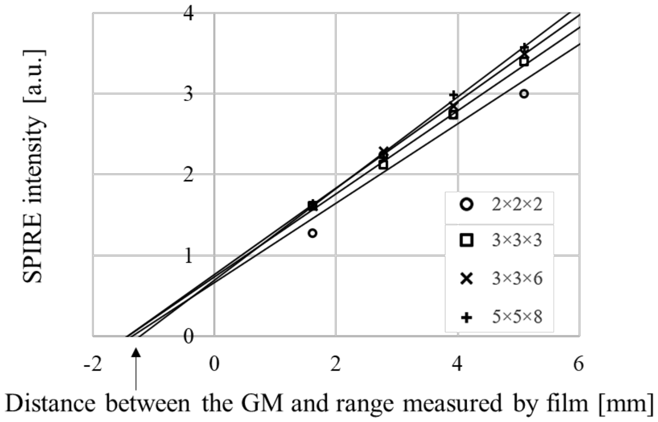


Figure 8. SPIRE intensity detected by four sizes of probe heads plotted against the distance between the GM and the range measured by the film.

*3.2 Range position detection*

*3.2.1 γ-wave*

The waveform comparisons at (a) distal and (b) lateral positions between the simulation and measurement are demonstrated in Figure 9 for the beam incident at $X = 0$, and the $t_{\gamma}^{peak}$ for the beam incident at $X = -30, -20, -10, 0, +10, +20, +30$ mm was shown in Figure 10. In Figure 10, the averaged data of 1000 samples were plotted with the error bars, which indicate the standard deviation (SD). Simulation results were plotted together. The delay due to the filter and amplifiers (1.98 μs) was subtracted from the measured data.

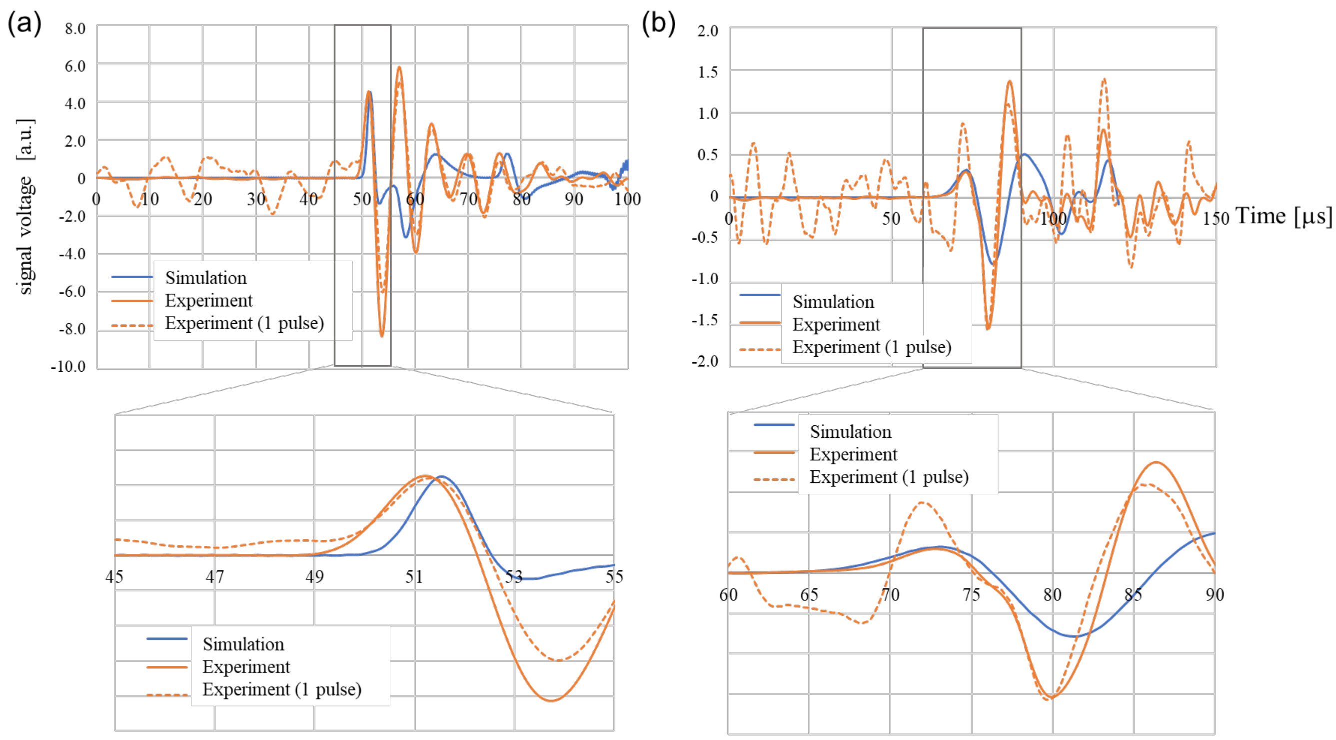


Figure 9. Comparison between the simulated and measured waveforms (blue solid curve: simulation, orange solid curve:1,000-fold averaging, and dotted curve: experiment (1-pulse)) observed at (a) distal and (b) lateral positions for the proton beam incident at $X = 0$. The figures below show enlarged views of the time ranges around the first peaks.

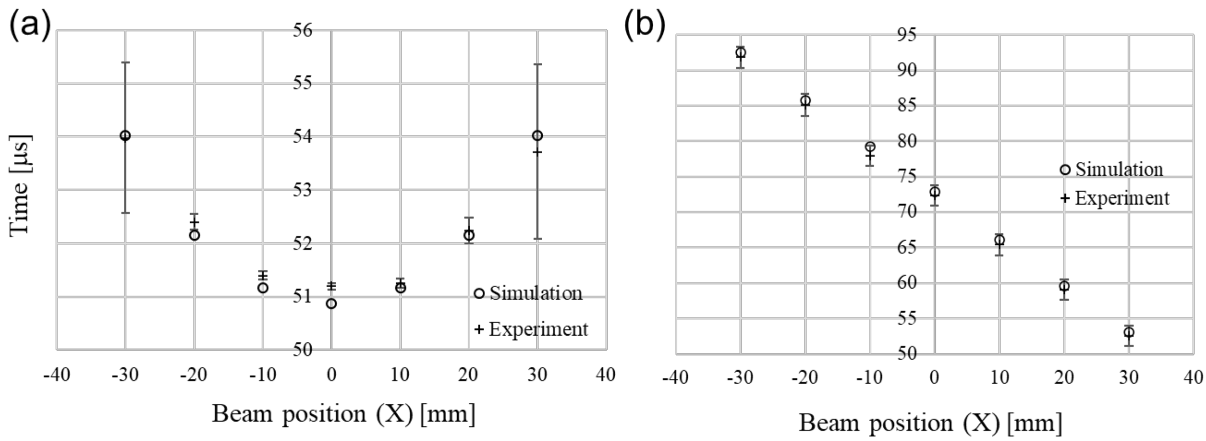


Figure 10. Comparison of the $t_\gamma^{peak}$ at (a) distal and (b) lateral positions for the beams incident at $X$ = −30, −20, −10, 0, +10, +20, and +30 mm. ○ and + indicate the simulation and experiment (1,000-fold averaging). The error bars indicate the SD over 1000 samples (0.3 Gy dose/sample) for the distal sensors. For lateral sensors, since we could not identify $t_\gamma^{peak}$ from the single pulse data, the SD of four-fold averaged data over 250 samples (1.2 Gy dose/sample) is shown.

The differences in $t_\gamma^{peak}$ between experiment and simulation were –0.3 to +0.3 µs and –1.2 to –0.5 µs at the distal and lateral positions, respectively. As shown in the Figure 10 (a) for distal sensors, the SD was less than 0.3 µs when the sensor was placed close to the beam axis (≤ 20 mm), but rapidly increased to about 1.5 µs when the sensor was 30 mm away from the beam axis. For lateral sensors, reflecting the small signal pressure, the SD of four-fold averaged samples was about 1.5 µs regardless of the sensor position.

Table 2 summarizes the differences in $t_{\gamma}^{peak}$ between the simulation and measurement ($\Delta \boldsymbol{t}$), sensitive matrix, and ($\Delta X, \Delta Z$). Table 3 shows $\Delta Z$ derived from a single distal sensor was shown with the dose required to suppress the SD <1 mm.

For the sensitivity of $t_{\gamma}^{peak}$ against the range shift, $\left|\frac{\partial t_{dist}}{\partial Z}\right|$ was at least three-fold larger than $\left|\frac{\partial t_{dist}}{\partial X}\right|$ for all tested beams (except for $X = 0$ where $\frac{\partial t_{dist}}{\partial X}$ is zero), whereas $\left|\frac{\partial t_{lat}}{\partial X}\right|$ is at least three-fold larger than $\left|\frac{\partial t_{lat}}{\partial Z}\right|$. An increase in $\frac{\partial t_{dist}}{\partial X}$ with the beam position ($X$) was observed, but no clear correlation with the beam positions was observed for other elements of the sensitive matrix.

For the range deviations, $|\Delta Z|$ was <1 mm for all tested beams in both cases using two sensors simultaneously and a single distal sensor. $\Delta X$ was between +0.6 to +1.2 mm except for the $X = -10$ mm beam. Since the variation of the $\Delta X$ values was small among different beams (≤0.6 mm), this may have been mainly caused from a systematic error, such as the phantom positioning error at the initial setup. We could not identify the cause of the large $\Delta X$ observed for the $X = -10$ mm beam, but it could be an input error to the potentiometer. When only a distal sensor was used for the range detection, the SD of $|\Delta Z|$ was <1 mm with a 0.3 Gy dose/pulse at $X = -30, -20, -10, 0, +10, +20$ mm, although a large dose of 0.6 Gy (dose at Bragg peak × number of pulses) was required when the sensor was positioned +30 mm away from the beam axis. In contrast, when the two sensors were simultaneously used to detect the beam range, the dose required to achieve the SD of $|\Delta X|$ and $|\Delta Z|$ <1 mm was increased to 1.2 Gy (dose at Bragg peak × number of pulses) since $t_{\gamma}^{peak}$ at lateral position could not be identified with a smaller dose.

Table 2. Summary of the difference in $t_{\gamma}^{peak}$ between the simulation and experiment ($\Delta \boldsymbol{t}$), sensitive matrix, the deviations of the range positions derived by γ-waves from those measured by the film ($\Delta Z$) and potentiometer ($\Delta X$).

| Beam position (mm) | $X$ | -30 | -20 | -10 | 0 | 10 | 20 | 30 |
|---|---|---|---|---|---|---|---|---|
| Difference of $t_{\gamma}^{peak}$ between exp. and sim. (μs) | $\Delta t_{dist}$ | -0.1 | 0.3 | 0.2 | 0.3 | 0.1 | 0.1 | -0.3 |
| | $\Delta t_{lat}$ | -0.7 | -0.6 | -1.2 | -0.5 | -0.6 | -0.6 | -0.6 |
| Sensitive matrix (μs/mm) | $\frac{\partial t_{dist}}{\partial X}$ | -0.2 | -0.1 | -0.1 | 0.0 | 0.1 | 0.1 | 0.2 |
| | $\frac{\partial t_{dist}}{\partial Z}$ | -0.6 | -0.7 | -0.7 | -0.6 | -0.7 | -0.7 | -0.6 |
| | $\frac{\partial t_{lat}}{\partial X}$ | -0.7 | -0.7 | -0.6 | -0.6 | -0.7 | -0.6 | -0.7 |
| | $\frac{\partial t_{lat}}{\partial Z}$ | -0.2 | -0.1 | -0.1 | -0.1 | -0.2 | -0.2 | -0.2 |
| Range deviation obtained by two sensors (mm) | $\Delta X$ | 1.2 | 1.0 | 2.1 | 0.9 | 0.9 | 1.0 | 0.6 |
| | $\Delta Z$ | -0.4 | -0.6 | -0.6 | -0.5 | 0.0 | 0.1 | 0.7 |

Table 3. Range deviation $\Delta Z$ obtained by a single distal sensor and the doses required to suppress the SD of $\Delta Z$ to <1 mm.

| Beam position (mm) | $X$ | -30 | -20 | -10 | 0 | 10 | 20 | 30 |
|---|---|---|---|---|---|---|---|---|
| Range deviation (mm) | $\Delta Z$ | 0.1 | -0.4 | -0.4 | -0.5 | -0.1 | -0.1 | 0.5 |
| Required dose to suppress both the SDs of $\Delta Z$ to <1 mm (Gy) | | 0.3 | 0.3 | 0.3 | 0.3 | 0.3 | 0.3 | 0.6 |

### *3.2.2 SPIRE*

Figure 11 shows the SPIRE intensity against the distance between the GM and the range measured by film (1,000-fold averaged). The intersection points between the linear functions fitted to the data points and the $x$-axis were −2.0 mm ($X$ = 0) and −1.9 mm ($X$ = 29 mm). By comparing these values with the simulated value derived in the previous study (−1.1 mm),[9] $\Delta Z$ was estimated 0.9 and 0.8 mm at $X$ = 0 and 29 mm, respectively.

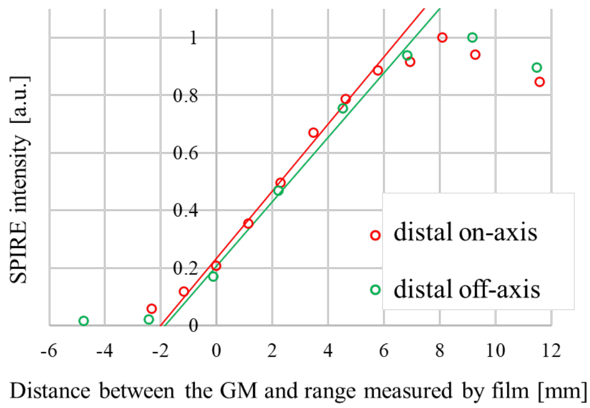


Figure 11. SPIRE intensity against the distance between the GM and the range measured by the film. Red and green circles refer to the data obtained at distal on-axis and off-axis (29 mm away from the beam axis) positions, respectively.

## *4. Discussion*

In this paper, we proposed the use of small probe head to exploit OH for the ionoacoustic range detection using a tissue-mimicking agar phantom. OH has advantages of a small size and high sensitivity; however, if the measurement is conducted on the phantom surface, the OH must be used with a probe head to prevent wave distortion due to the contamination of reflected waves from the sensor-air boundary. Though we used an agar block for the probe head, the use of more durable materials, such as PVCP, commonly employed as a tissue-mimicking phantom,[27] would be more appropriate for the probe head. However, we assumed that this would not affect the outcome of this study. Unlike a PH, the probe head is made of low-Z material and the sensitive volume is still point-wise even with the probe head, allowing the simple waveform analysis employed here. We demonstrated by experiment that at the distal on-axis position, $t_{\gamma}^{peak}$ and the predicted beam range by SPIRE did not differ among the investigated probe heads. Although the smallest probe head (2 × 2 × 2 $cm^3$) showed the signal reduction and the $t_{\gamma}^{peak}$ shift at the distal off-axis position, the second smallest probe head (3 × 3 × 3 $cm^3$) did not (Figure 6); hence, we consider the 3 × 3 × 3-$cm^3$ probe head may be adequate for the use of range detection. For the SPIRE, we assumed that the experimental results for the distal on-axis position hold for other sensor positions since the waveform of the SPIRE is in principle spherically symmetric and the diffraction at the probe head edge is smaller at MHz regime; however, this needs to be confirmed by the future experiments. Placing the sensitive volume closer to the probe head surface, adding the acoustic absorbers to the probe head walls, and further optimizing the probe head shape may allow further reduction of wave distortion.

The beam range in this study was derived by solving the linear equation $\Delta\boldsymbol{X} = \boldsymbol{S}^{-1}\Delta\boldsymbol{t}$ when the two γ-waves were used. The measurement condition of this study is a specific case where the dimension of the measured values ($\Delta\boldsymbol{t}$) was equal to the number of parameters to be identified ($\Delta\boldsymbol{X}$) and the sensitive matrix was invertible. For general cases, where the number of measurement points differs from the dimension of $\Delta\boldsymbol{X}$, the sensitive matrix becomes noninvertible. In this case, $\Delta\boldsymbol{X}$ that approximately reproduces the measured values ($\Delta\boldsymbol{t}$) is derived by the least square method, and the solution is reduced to $\Delta\boldsymbol{X} = (\boldsymbol{S}^{\boldsymbol{T}}\boldsymbol{S})^{-1}\boldsymbol{S}^{\boldsymbol{T}}\Delta\boldsymbol{t}$. In principle, the present range detection method could be used even if the phantom is acoustically heterogeneous. Moreover, the results do not rely on the definition of time of flight used, which sometimes leads to Bragg peak localization errors.[19] Alternatively, its use is limited to the cases when the actual range position is close to the reference point used in the simulation ($\boldsymbol{X}^{\boldsymbol{sim}}$). For instance, given that when the beam is shifted from $X = 0$ to

30 mm at a 10-mm pitch using the translation stage and $\boldsymbol{X}^{sim}$ = (0, 73.9 mm) was retained as the reference point, $|\Delta Z|$ was <1 mm for $X$ = 0 and 10 mm beams but increased to 2.3 and 3.3 mm for $X$ = 20 and 30 mm beams, respectively. Hence the reference point should be as close to the true range position as possible. A natural candidate for the reference point is the maximum dose point estimated by dose calculation using the CT of the patient. However, when the uncertainty of dose distribution on the patient CT is large, the point that is derived by the one-way beamforming[17] or multilateration method[18,28] would be another choice if multiple OHs could be used.

As shown in Figure 9, although the ionoacoustic wave simulation could reproduce $t_{\gamma}^{peak}$, the simulated waveform largely differed from that in the experiment after the first intersection point with the time-axis. This may be partly because the simulation did not model the internal structures of the hydrophone as well as the frequency response of the detector, however, the exact cause is not clear at this point. The waveform after the first peak is useful especially when the 3D dose distribution is reconstructed from multiple sensors,[6,29] and it is therefore desirable to improve the simulation accuracy. A possible approach was proposed by Schauer et al.,[14] who measured total impulse response function using optoacoustics. The extensive study of their method on OH is worth to be investigated in the future.

Although the γ-wave is sometimes described as a spherical wave, the intensity is not spherically symmetric, especially when a low-energy beam is used as in this study, where the gradient of the Bragg peak is sharp in the distal direction; in this situation, the intensity is high at the distal on-axis and then rapidly decreases away from the axis. Fortunately, the region where the high-intensity waves arrive coincides with the region that has the highest sensitivity against the range shift in the $Z$ direction. As clinical machines measure the $XY$ positions precisely during beam delivery by the multiwire chambers, the most important parameter to verify is $Z$, and so the measurement at distal positions should add the greatest clinical value. In practice, since the beam is scanned several centimeters across the target tumors, it may be desirable to deploy a two-dimensional OH array covering several centimeters at the distal on-axis regime and use the waveforms that have sufficient SNR to identify $\Delta Z$ for each beam. The optimum sensor spacings and array sizes need to be determined in the future. By contrast, SPIRE is advantaged in that it is almost omnidirectional; however, the sensitivity of the OH in the MHz region was insufficient to identify the beam range with a clinical dose (frequency response of OH is presented in the Supplementary Material).[9] Additionally, since the SPIRE has a small wavelength of about 1 mm, its signal strength is sensitive to OH orientation relative to the radial wave propagation. Thus, overcoming these limitations remains a future challenge for clinical use.

Another limitation of this research includes the use of a nonclinical machine of a fixed-field alternating gradient accelerator, although this is a candidate accelerator for future proton therapy. In addition, the beam energy was limited to a relatively low energy of 100 MeV. Clinical accelerators generally have a longer pulse duration, and a higher energy beam generates a broader Bragg peak due to the range straggling; therefore, a larger dose would be necessary to achieve a sufficiently large SNR in clinical conditions. In addition, moving toward clinical implementation, further investigation is needed to establish the appropriate speed of sound correction and accurate positioning of the probe heads.

## *5. Conclusions*

This paper demonstrated a prototype OH probe head that could detect the initial segment of the ionoacoustic wave without distortion on the tissue-mimicking phantom surface. The relatively small-sized $3 \times 3 \times 3$-cm$^3$ probe head could prevent the wave distortion of the $\gamma$–wave if the detection was performed within 3 cm from the beam axis at distal positions. The range in depth direction was derived with submillimeter accuracy within clinical dosage (0.3–0.6 Gy at the Bragg peak) by using a distal sensor, although the required dose was increased to 1.2 Gy if the lateral sensor was included to identify both the $X$ and $Z$ positions of the range. The range could also be measured with a small-sized probe head from SPIRE measurement at distal positions; however, the sensitivity of OH in the MHz regime needs to be improved toward clinical use.

**Acknowledgments**

We thank Cristiano Tomasi, Dr. Morita and Rina Tohyama for their professional support, Mrs. Tomoki Uesaka and Yuta Nakamura for valuable discussions. This research was supported by JSPS KAKENHI grant no. 21K19434 and the JST FOREST Program (grant no. JPMJFR200X, Japan).

**Conflicts of interest statement**

Taisuke Takayanagi is paid by Hitachi Ltd., Tokyo, Japan, and Wolfgang Rohringer is paid by XARION Laser Acoustics GmbH, Vienna, Austria. Other authors have no conflicts of interest.

**Data availability**

Data supporting the findings of this study are available from the corresponding author upon reasonable request.

**References**

1. Jones KC, Witztum A, Sehgal CM, Avery S. Proton beam characterization by proton-induced acoustic emission: simulation studies. *Phys Med Biol*. 2014;59(21):6549-6563. doi:10.1088/0031-9155/59/21/6549.
2. Hayakawa Y, Tada J, Arai N, et al. Acoustic pulse generated in a patient during treatment by pulsed proton radiation beam. *Radiat Oncol Investig*. 1995;3(1):42-45. doi:10.1002/roi.2970030107.

3. Hickling S, Xiang L, Jones KC, et al. Ionizing radiation-induced acoustics for radiotherapy and diagnostic radiology applications. *Med Phys*. 2018;45(7):e707-e721. doi:10.1002/mp.12929.

4. Assmann W, Kellnberger S, Reinhardt S, et al. Ionoacoustic characterization of the proton Bragg peak with submillimeter accuracy. *Med Phys*. 2015;42(2):567-574. doi:10.1118/1.4905047.

5. Kellnberger S, Assmann W, Lehrack S, et al., Ionoacoustic tomography of the proton Bragg peak in combination with ultrasound and optoacoustic imaging. Sci Rep. 2016;6:29305. doi: 10.1038/srep29305.

6. Lascaud J, Dash P, Wieser HP, et al. Investigating the accuracy of co-registered ionoacoustic and ultrasound images in pulsed proton beams. *Phys Med Biol*. 2021;66(18). doi:10.1088/1361-6560/ac215e.

7. Schauer J, Wieser HP, Huang Y, et al. Proton beam range verification by means of ionoacoustic measurements at clinically relevant doses using a correlation-based evaluation. *Front Oncol*. 2022;12:925542. doi:10.3389/fonc.2022.925542.

8. Takayanagi T, Uesaka T, Nakamura Y, et al. On-line range verification for proton beam therapy using spherical ionoacoustic waves with resonant frequency. *Sci Rep*. 2020;10(1):20385. doi:10.1038/s41598-020-77422-2.

9. Sueyasu S, Takayanagi T, Miyazaki K, et al. Ionoacoustic application of an optical hydrophone to detect proton beam range in water. *Med Phys*. 2023;50(4):2438-2449. doi:10.1002/mp.16189.

10. Jones KC, Vander Stappen F, Sehgal CM, Avery S. Acoustic time-of-flight for proton range verification in water. *Med Phys*. 2016;43(9):5213. doi:10.1118/1.4961120.

11. Lehrack S, Assmann W, Bertrand D, et al. Submillimeter ionoacoustic range determination for protons in water at a clinical synchrocyclotron. *Phys Med Biol*. 2017;62(17):L20-L30. doi:10.1088/1361-6560/aa81f8.

12. Patch SK, Nguyen C, Dominguez-Ramirez D, et al. Thermoacoustic range verification during pencil beam delivery of a clinical plan to an abdominal imaging phantom. *Radiother Oncol*. 2021;159:224-230. doi:10.1016/j.radonc.2021.03.027.

13. Caron J, Gonzalez G, Pandey PK, et al. Single pulse protoacoustic range verification using a

clinical synchrocyclotron. *Phys Med Biol*. 2023;68(4). doi:10.1088/1361-6560/acb2ae.

14. Schauer J, Wieser HP, Lascaud J, et al. Range verification of a clinical proton beam in an abdominal phantom by co-registration of ionoacoustics and ultrasound. *Phys Med Biol*. 2023 [Epub ahead of print];68(12). doi:10.1088/1361-6560/acd834.
15. Lascaud J, Kalunga R, Lehrack S, et al. Applicability of capacitive micromachined ultrasonic transducers for the detection of proton-induced thermoacoustic waves. IEEE Int Ultrasonics Symposium; 2019:143-146. doi:10.1109/ULTSYM.2019.8926023.
16. van der Heiden MS, van Neer P, Wieser HP, et al. *Ultrasensitive Optoacoustic Sensor for Dosimetry in Proton Therapy-OMUS4PT*.
17. Patch SK, Santiago-Gonzalez D, Mustapha B. Thermoacoustic range verification in the presence of acoustic heterogeneity and soundspeed errors – Robustness relative to ultrasound image of underlying anatomy. *Med Phys*. 2019;46(1):318-327. doi:10.1002/mp.13256.
18. Kalunga R, Wieser HP, Dash P, et al. On the robustness of multilateration of ionoacoustic signals for localization of the Bragg peak at pre-clinical proton beam energies in water. *Phys Med Biol*. 2023;68(10):105010. doi:10.1088/1361-6560/acc9f7.
19. Shimizu S, Miyamoto N, Matsuura T, et al. A proton beam therapy system dedicated to spot-scanning increases accuracy with moving tumors by real-time imaging and gating and reduces equipment size. *PLOS ONE*. 2014;9(4):e94971. doi:10.1371/journal.pone.0094971.
20. Hoffmann A, Oborn B, Moteabbed M, et al. MR-guided proton therapy: a review and a preview. *Radiat Oncol*. 2020;15(1):129. doi:10.1186/s13014-020-01571-x.
21. Wissmeyer G, Pleitez MA, Rosenthal A, Ntziachristos V. Looking at sound:optoacoustics with all-optical ultrasound detection. *Light Sci Appl*. 2018;7:53. doi:10.1038/s41377-018-0036-7.
22. Ishi Y. Status report on FFAG accelerator complex at KURRI. *Proc of the 12th Annual Meeting of Particle Accel Soc of Japan*. 2015;368-370.
23. Kuriyama Y. Status and development of a proton FFAG accelerator at KURRI for ADSR study. *Proc of 2011 Particle Accelerator Conference*. THP027; 2011:2172-2174.
24. Preisser S, Rohringer W, Liu M, et al. All-optical highly sensitive akinetic sensor for ultrasound

detection and photoacoustic imaging. *Biomed Opt Express*. 2016;7(10):4171-4186. doi:10.1364/BOE.7.004171.

25. Allison J, Amako K, Apostolakis J, et al. Recent developments in GEANT4. *Nucl Instrum Methods A*. 2016;835:186-225. doi:10.1016/j.nima.2016.06.125.
26. Treeby BE, Cox BT. k-Wave: MATLAB toolbox for the simulation and reconstruction of photoacoustic wave fields. *J Biomed Opt*. 2010;15(2):021314. doi:10.1117/1.3360308.
27. Spirou GM, Oraevsky AA, Vitkin IA, Whelan WM. Optical and acoustic properties at 1064 nm of polyvinyl chloride-plastisol for use as a tissue phantom in biomedical optoacoustics. *Phys Med Biol*. 2005 21;50(14):N141-N153. doi:10.1088/0031-9155/50/14/N01.
28. Otero J, Felis I, Ardid M, Herrero A. Acoustic Localization of Bragg Peak Proton Beams for Hadrontherapy Monitoring. Sensors (Basel). 2019 Apr 26;19(9):1971. doi: 10.3390/s19091971.
29. Yu Y, Qi P, Peng H. Feasibility study of 3D time-reversal reconstruction of proton-induced acoustic signals for dose verification in the head and the liver:a simulation study. *Med Phys*. 2021;48(8):4485-4497. doi:10.1002/mp.15046.